

Medical Image Denoising via Explainable AI Feature Preserving Loss

Guanfang Dong
Multimedia Research Center
University of Alberta
guanfang@ualberta.ca

Anup Basu
Multimedia Research Center
University of Alberta
basu@ualberta.ca

Abstract—Denoising algorithms play a crucial role in medical image processing and analysis. However, classical denoising algorithms often ignore explanatory and critical medical features preservation, which may lead to misdiagnosis and legal liabilities. In this work, we propose a new denoising method for medical images that not only efficiently removes various types of noise, but also preserves key medical features throughout the process. To achieve this goal, we utilize a gradient-based eXplainable Artificial Intelligence (XAI) approach to design a feature preserving loss function. Our feature preserving loss function is motivated by the characteristic that gradient-based XAI is sensitive to noise. Through backpropagation, medical image features before and after denoising can be kept consistent. We conducted extensive experiments on three available medical image datasets, including synthesized 13 different types of noise and artifacts. The experimental results demonstrate the superiority of our method in terms of denoising performance, model explainability, and generalization.

I. INTRODUCTION

Medical image denoising is an important stage in medical image processing and analysis. Its main objective is to remove noise from a medical image while retaining key information about lesions and structures [1]. Unlike conventional image denoising algorithms, medical image denoising requires a judicious and transparent approach to noise removal. The improper or unexplained removal of noise may lead to misleading diagnosis, lack of trust, and legal and ethical liabilities [2]. Therefore, we are motivated to propose a new method that effectively removes all types of noise, while preserving key medical image features and providing explainability.

In order to preserve critical medical features during the denoising process, we leverage the potential of eXplainable Artificial Intelligence (XAI). XAI is a broader research topic that aims to improve the transparency, explainability, and trustworthiness of AI systems. In this work, we adopt a gradient-based XAI approach to extract the medical image features. In general, gradient-based XAI explains the model behaviour by exploiting gradient information during backpropagation of deep neural networks.

In this work, we employ a deep learning model for image restoration task, represented by a function f . This function maps an input image x to a restored output image y : $y = f(x)$. Gradient-based XAI is used to identify which regions of the input image x contribute the most significantly to the output image

y . To achieve this, we can compute the gradient of the model output y with respect to the input x , denoted as ∇x .

Since the model output is a continuous value, the elements of the gradient ∇x reflect the contribution of each component in the input image x to the restored output image y . A larger gradient value indicates a greater influence of the input component on y .

Gradient-based XAI methods have some limitations; one of the drawback is their sensitivity to noise. The explanation result may be affected by noise due to the sensitivity of gradients to small changes in the input, leading to misleading explanations. In many cases, this property is perceived as a drawback that gradient-based XAI methods must overcome. Nevertheless, we find that this attribute provides a potential for feature preservation in denoising networks. Due to this limitation, the features of a clean medical image and a noisy medical image differ from each other. Consequently, we can design a loss function that guides the network to fit the features of a clean medical image. It is important to highlight that the gradient features obtained for clean and noisy images can be visualized using a saliency map. This introduces explainability to our approach. Although the features extracted by XAI slightly differ from the actual medical image features, we are still able to obtain explanations for the model’s denoising behavior. To some extent, the trust problem associated with black-box neural network models is alleviated.

Our method is robust to different types of noise. Furthermore, our method demonstrates the capability to generalize across various medical image acquisition devices. To validate these claims, we conducted extensive experiments. Initially, our denoising experiments employed three publicly available datasets. They are the Lung Image Database Consortium image collection (LIDC-IDRI), RSNA Pneumonia Detection, and LiTS (Liver Tumor Segmentation), covering both CT and X-ray image acquisition devices. At the same time, we simulated 13 different types of noise or artifacts, including Gaussian noise, Poisson noise, speckle noise, non-central chi-square noise, Rayleigh noise, salt-and-pepper noise, structure noise, thermal noise, magnetic field inhomogeneity noise, chemical shift artifact, motion artifact, wrap artifact, and susceptibility artifact. Both the denoising and artifact removal results demonstrated that our method achieves good denoising performance.

Overall, our contributions are as follows:

- 1) We propose a feature preserving loss that utilizes the potential of gradient-based XAI method. We leverage its sensitivity to noise to design a loss function. This loss function can guide the denoising network to fit the features of clean medical images.
- 2) The feature preserving loss improves the explainability of the denoising network, allowing users to visualize the medical features before and after the denoising is applied.
- 3) We perform extensive denoising experiments on large-scale medical imaging datasets and 13 different noise type. The experimental results demonstrate the robustness and generalizability of the feature preservation loss. The importance of preserving important information is thus proved.

II. RELATED WORK

Denoising is a fundamental processing step in image processing. The primary objective of denoising algorithms is to remove image noise while preserving critical features within the image, such as edges and textures. Many well-known denoising algorithms aim to address this issue. Mean Filtering [3] removes noise by substituting each pixel's value with the average value of its neighboring pixels. Median Filtering [4] alleviates noise by replacing the current pixel value with the median value among its neighbors. Gaussian Filtering [5] operates in the spatial domain, utilizing Gaussian functions as weights in convolution. Wiener Filtering [6] is an optimal filtering technique that minimizes the square of the error. Wavelet Transform employs multi-scale approaches for denoising [7].

However, in medical image denoising, classical algorithms encounter multiple challenges. To efficiently eliminate noise, classical algorithms may remove both subtle structures and important features within the image, which is unacceptable in medical diagnostics. Also, denoising medical images necessitates higher computational complexity. Therefore, algorithms with high computational complexity, such as BM3D [8], struggle to be applied on high-resolution medical images. Then, different types of medical images (e.g., MRI, CT, X-ray, etc.) have different noise distributions. This requires denoising algorithms to tune the parameters manually. Unfortunately, most traditional algorithms lack adaptivity. Since noise has a complex dependence on the signal, this makes linear denoising methods ineffective.

Therefore, in recent years, more research has focused on medical image denoising using machine learning and deep learning methods. Although learning-based methods have obvious advantages in adapting to different noise models, they also introduce new problems such as overfitting and poor interpretability. Zhang et al. [9] proposed a CNN denoiser prior, called DPIR, that can handle various noise levels. DPIR is applicable to interpolative image restoration methods. Neshatavar et al. [10] proposed a self-supervised denoising method called CVF-SID. CVF-SID is based on a cyclic multivariate function module and a self-supervised image disentanglement framework. However, although these recent works have considered different noise distributions, they do

not consider feature extraction for noisy images. Especially in medical image denoising, the lack of feature consideration will result in over-smoothing of the denoised images. For this reason, Dong et al. [11] proposed FDCNN, which uses medical features as guidance and combines them with the denoised image through fusion. However, although their method successfully preserves medical features, it cannot eliminate noise in the feature areas. Their work motivates us to propose a method that not only preserves the features but also denoises the feature areas.

III. METHODOLOGY

As shown in Fig. 1, we propose a multi-stage medical image denoising method that combines image restoration, explanation and denoising. Our method first uses a pre-trained image restoration network. This network maps the noise-free medical images I_{clean} to the same noise-free image space. Next, a gradient-based explainable artificial intelligence (XAI) technique, Guided Back-Propagation [12], is used to explain the output of the image restoration network. After the pre-training image restoration network is well trained, we train the image denoising network. The input to the denoising network is an image I_{noise} corrupted by applying various noise masks M_{noise} . During the training phase, both I_{noise} before denoising and I_{denoise} after denoising are passed through the gradient-based XAI. So, the corresponding medical image features F_{denoised} and F_{clean} are extracted. Subsequently, the network minimizes the feature differences between F_{denoised} and F_{clean} . This allows critical medical features to be preserved in the denoising process. With F_{denoised} and F_{clean} are been visualized, we also allow medical experts to explain and trust the model outputs. More implementation details will be covered in the following subsections.

A. Gradient-based XAI and Sensitivity to Noise

Gradient-based XAI methods focus on utilizing gradient information from neural networks to explain model decisions for a given input. Saliency Maps [13], Grad-CAM [14], Guided Back-propagation [12], etc. are typical methods for Gradient-based XAI. While these methods are slightly different, their basic idea is to calculate the gradient of the model output relative to the input. The calculated gradient is then used to quantify how much the input features affect the output. Mathematically, for a neural network f and an input x . Gradient-based XAI computes $\frac{\partial f(x)}{\partial x}$ to explain the decision of the model. Although this method is simple and intuitive, it potentially faces some problems, such as sensitivity to noise.

To demonstrate the sensitivity, we consider a layer of neural network:

$$f(x) = \sigma(w \cdot x + b), \quad (1)$$

where σ is the Sigmoid activation function. w and b are the weight and bias. x is the input. We slightly add some noise to x . So, the new input will be $x' = x + \epsilon$. In this case, the result of neural network will be $f(x') = \sigma(w \cdot (x + \epsilon) + b)$. Now, we compute the gradient for x and x' . Since derivative of

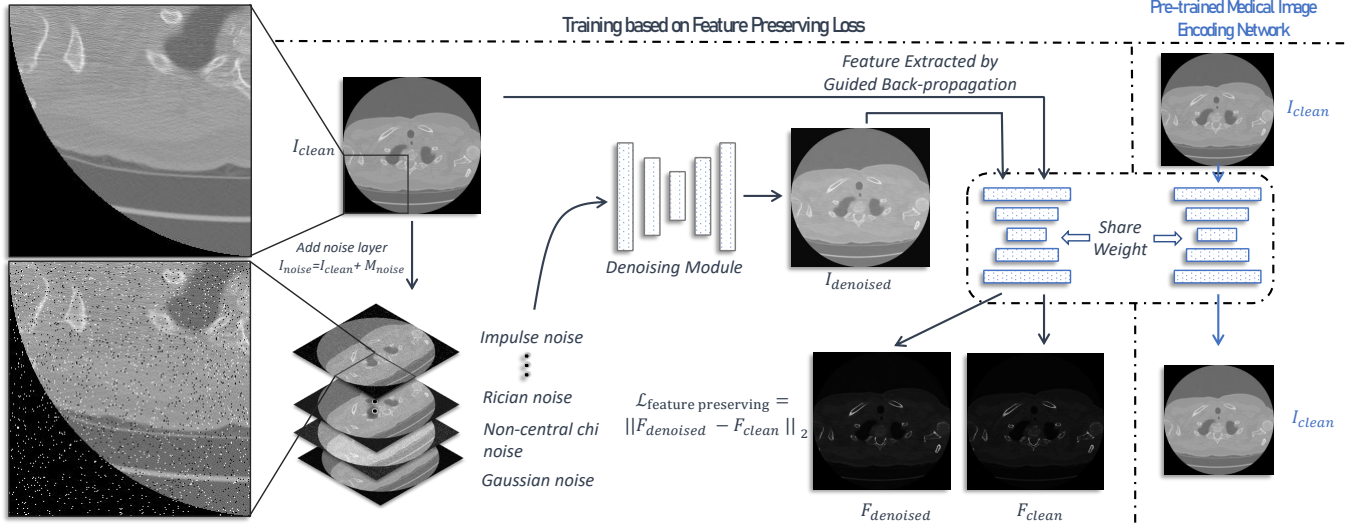


Fig. 1: Workflow of the Proposed Method.

the Sigmoid function is $\sigma'(x) = \frac{d}{dx} \left(\frac{1}{1+e^{-x}} \right) = \frac{e^{-x}}{(1+e^{-x})^2} = \sigma(x) \cdot (1 - \sigma(x))$, we can clearly see that even a slightly ϵ will lead the big change in $\sigma'(x)$ if x closes to 0. Also, this change might be amplified by w since the gradient of the input is computed as $\frac{df}{dx'} = w \cdot \sigma'(w \cdot (x + \epsilon) + b)$.

Although this property is seen as a drawback in most cases, we are exploiting it to force the network to learn the difference between medical image features with and without noise. Therefore, for the choice of gradient-based XAI methods, we did not choose methods such as SmoothGrad [15] or Integrated Gradients [16], which suppress noise sensitivity. We choose Guided Back-Propagation in this work. In standard backpropagation, gradients are automatically propagated through the computational graph. However, in Guided Backpropagation, the propagation of the gradient is constrained, especially in the case of ReLU activation functions. Mathematically, assuming that R is the gradient propagated from the previous layer, the Guided Backpropagation update in case of ReLU activation as follows:

$$R_{updated} = R \odot \left(\frac{\partial f(x)}{\partial x} > 0 \right) \odot (x > 0), \quad (2)$$

where R is the original gradients, $\frac{\partial f(x)}{\partial x}$ is the gradient with respect to the input x , \odot is the element-wise multiplication. $\frac{\partial f(x)}{\partial x} > 0$ is an indicator, determining whether the model is positively or negatively activated. $x > 0$ determines the input x is positive or negative. Thus, during backpropagation, only gradients satisfy both positive model activations and inputs are retained. In this way, the updated importance scores will contain only those features that contribute positively to the model predictions. By visualizing this, an intuitive and useful explanation can be provided.

B. Feature Preserving Loss

Based on the discussion of Section III-A, we can assume a differentiable feature extraction method ϕ that utilizes the Guided Back-propagation. For a corrupted medical image $I_{noise} \in \mathbb{R}^{h \times w}$, it can be considered as an overlay of a noise mask M_{noise} and a clean image I_{clean} . Mathematically, it can be written as $I_{noise} = M_{noise} + I_{clean}$. Thus, for a pixel $I_{noise}(x, y)$ that locates at I_{noise} at position x and y , there are three possible cases.

- 1) The pixel is only consist by noise, namely $I_{noise}(x, y) = M_{noise}(x, y)$.
- 2) The pixel is only consist by medical feature, namely $I_{noise}(x, y) = I_{clean}(x, y)$.
- 3) The pixel is consist with noise and medical feature, namely $I_{noise}(x, y) = M_{noise}(x, y) + I_{clean}(x, y)$.

Let's recall the concept of feature importance weight $F \in \mathbb{R}^{h \times w}$ derived from gradient-based XAI, specifically from guided back-propagation. For each pixel at (x, y) , $F(x, y)$ quantifies the contribution of that pixel to a specific medical feature in the medical image.

The feature preserving loss, denoted as L_{FP} , can be defined mathematically as follows:

$$L_{FP} = \sum_{x,y} \|F_{denoised}(x, y) - F_{clean}(x, y)\|^2, \quad (3)$$

where $F_{denoised}$ is the output of guided backpropagation for denoised image, F_{clean} is the output of guided backpropagation for clean image, and $\|\cdot\|^2$ denotes the squared Euclidean norm.

Traditional loss functions and training methods such as mean square error (MSE) and residual learning work well for the first two cases (purely noisy and purely medical feature pixels). This is because the mean square error helps the

neural network to globally model and learn the pattern and distribution of the noise. However, when traditional denoising methods encounter the third case, both MSE and residual learning are not specifically designed to distinguish between features and noise within the same pixel. They minimize the global difference between denoised and clean images, but this often comes at the cost of losing local features that are critical for medical diagnosis. This is because of the convolutional operations that may be used by neural networks in optimizing MSE. Especially in medical images, adjacent pixels tend to have similar brightness and color. In the process of minimizing MSE, the model will tend to maintain this local consistency and therefore may smooth the medical features.

The feature preserving loss makes the neural network more concerned about the feature weights on the medical image features. Since the feature preserving loss is obtained by using gradient-based explainable method, it takes into account the importance of each pixel independently. Thus making the neural network more focused on local features rather than global smoothing.

C. Network Structure

We use the two identical U-Net network architectures for gradient-based XAI feature extraction and image denoising. Since the U-Net architecture [17] is not our contribution, we discuss it briefly. U-net consists of a symmetric encoder-decoder structure and an output convolutional layer. The input data is first passed through a feature extraction layer using a 3×3 convolutional kernel and keeping the number of output channels at 64. Subsequently, the encoder starts downsampling through four ‘Down’ modules, where each ‘Down’ module consists of a maximum pooling layer and a double convolution, activated by ReLu. The number of channels is gradually increased from 64 to 128, 256, and 512 to capture higher-level semantic information.

The output of the encoder is then passed to the decoder which is upsampled by four ‘Up’ modules. In this process, the feature maps corresponding to the layers of the encoder are concatenated with the output of the decoder. The number of channels is gradually reduced from 512 to 256, 128, 64, and finally 1 output channel is generated at the output layer by a 1×1 convolutional kernel.

Except feature preserving loss L_{FP} , we also applied the classic residual loss function for the purpose of denosing non-feature loss. Residual loss is commonly used to quantify the difference between the network output and the original clean signal, taking into account the noise component. Specifically, we have noisy image I_{noise} , corresponding clean image I_{clean} . $I_{denoised}$ is the output of the denoising module. The residual r is defined as the difference between the denoised image and the noisy image:

$$r = I_{noise} - I_{denoised} \quad (4)$$

The residual loss L_{res} is defined as the square of the difference between the residual r and the actual noise mask

M_{noise} .

$$L_{res}(r, M_{noise}) = \|r - M_{noise}\|^2, \quad (5)$$

IV. EXPERIMENTAL RESULT

In this section, we first provide the overview about the medical imaging dataset, applied noising types, evaluation metrics and implementation details. Then, we demonstrate the effectiveness of proposed feature preserving loss quantitatively and qualitatively. Moreover, we conclude a in-depth discussion about the explainability that been provided by feature preserving loss.

A. Medical Imaging Dataset

To demonstrate the robustness of proposed loss function towards different acquisition equipments. Three public medical imaging dataset are been used. They are Lung Image Database Consortium image collection (LIDC-IDRI) [18], RSNA Pneumonia Detection [19] and LiTS - Liver Tumor Segmentation [20].

LIDC-IDRI: Lung Image Database Consortium Image Collection (LIDC-IDRI) [18] is a publicly available medical image database. It focuses on early diagnosis and detection of lung cancer. LIDC-IDRI includes 1018 cases totaling more than 20,000 Computed Tomography (CT) images. Each case typically includes a series of slice images that are used to form a three-dimensional representation of the lung structure. These images are stored in DICOM (Digital Imaging and Communications in Medicine) format.

RSNA: RSNA Pneumonia Detection [19] is a dataset used in medical image analysis competitions. The dataset typically consists of about 30,000 chest X-ray images that are categorized as either positive or negative for pneumonia.

LiTS: LiTS (Liver Tumor Segmentation) [20] is a medical imaging database dedicated to liver and liver tumor segmentation. LiTS datasets typically contain approximately 130 liver cases, each consisting of a series of consecutive computed tomography (CT) slices.

For the purpose of comparison, we randomly choose 5,000 images from each dataset for training. The images are reshaped to (256×256) . Then, 500 images are randomly selected for testing purpose.

B. Types of Synthesized Noise and Artifacts

To evaluate the robustness of the proposed Feature Preserving Loss, we employ 13 common noise and synthetic artifacts in the medical image. Figure 2 shows the some of the sample noises. Also, Table I summarizes the 13 different noises and artifacts that applied in our experiment.

C. Evaluation Metric

Similar to other regular denoising metrics, we use Peak Signal-to-Noise Ratio (PSNR) and Structural Similarity Index (SSIM) as evaluation metrics. The inputs for the computing PSNR and SSIM are the original image I_{clean} and the denoised image $I_{denoised}$.

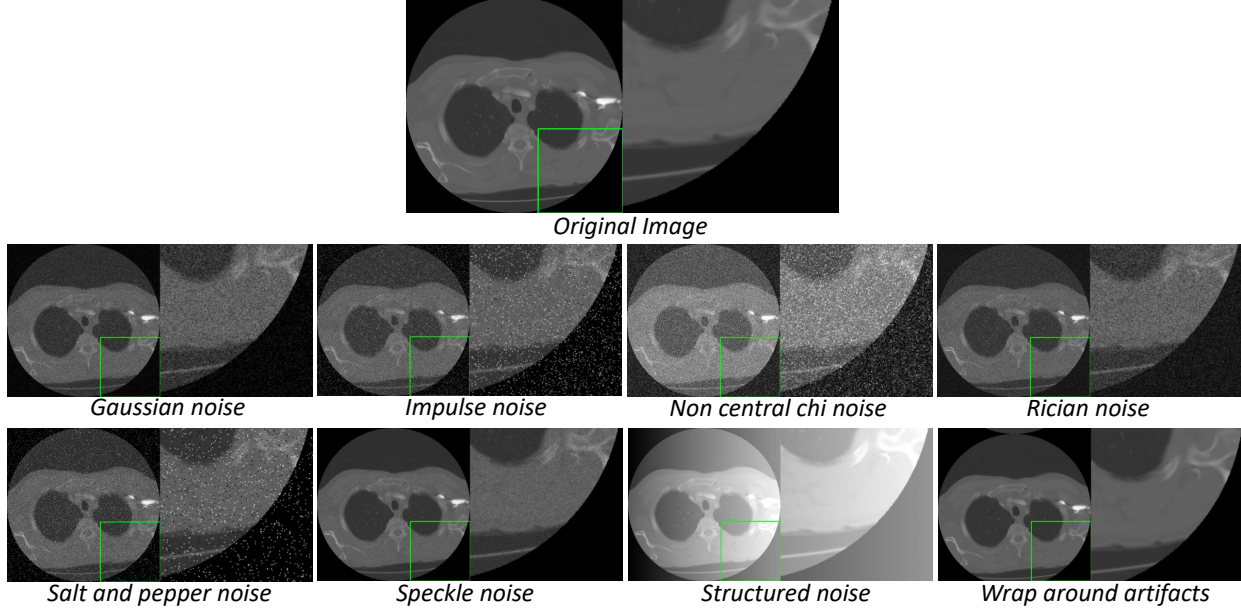


Fig. 2: Sample images for synthesized noises.

PSNR is a metric used to measure the difference between the original image and the denoised image. The higher its value, the better the denoising effect. PSNR is defined as

$$\text{PSNR} = 10 \cdot \log_{10} \left(\frac{\text{MAX}_I^2}{\text{MSE}} \right), \quad (6)$$

where MAX_I is the maximum possible pixel value of the image (e.g., for an 8-bit image, $\text{MAX}_I = 255$), and MSE is the mean-square error, computed as

$$\text{MSE} = \frac{1}{m \cdot n} \sum_{i=0}^{m-1} \sum_{j=0}^{n-1} (I_{\text{clean}}(i, j) - I_{\text{denoised}}(i, j))^2, \quad (7)$$

where m and n are the dimensions of the image.

SSIM is used to measure the structural similarity of two images. SSIM takes into account the brightness, contrast and structural information. The value of SSIM ranges from -1 to 1. The closer the value is to 1, the better the denoising effect. SSIM is defined as

$$\text{SSIM}(x, y) = \frac{(2\mu_x\mu_y + c_1)(2\sigma_{xy} + c_2)}{(\mu_x^2 + \mu_y^2 + c_1)(\sigma_x^2 + \sigma_y^2 + c_2)}, \quad (8)$$

where x and y are the I_{clean} and I_{denoised} . μ_x and μ_y are the mean values of the images. σ_x^2 and σ_y^2 are the variances of the images, σ_{xy} is the covariance of the image, c_1 and c_2 are constants to prevent the denominator from being zero.

D. Quantitative Evaluation

Tables II, III and IV demonstrate the evaluate results for dataset LIDC, LiTs and RSNA. We compare our method

with 9 common denoising methods under different noise and artifact conditions. To save space on the table, we use abbreviations. The correspondence is DPIP: Deep Plug-and-Play Image Restoration; Bilat.: Bilateral Filter; Filt. Comb.: Combined denoising strategies by Mean Filter, Median Filter and Gaussian Filter; Gaus. Filt.: Gaussian Filter; Mean Filt.: Mean Filter; Medi Filt.: Median Filter; NL Mean.: Non-local Means Denoising; Wave. Den.: Wavelet Denoising; Wien. Filt.: Wiener Filter.

Among them, DPIP [9] is the deep learning advanced-performed denoising algorithm. In three different datasets, DPIP is the best method other than our proposed method in most cases. Although the DPIP algorithm has considered Noise Level Map for preprocessing, this approach still has limitations in processing medical images. Specifically, it is difficult for the Noise Level Map to capture various local features and the corresponding feature intensities in medical images. This causes the algorithm perform poorly when dealing with noises that are particularly destructive to medical features, such as non-central Chi noise. Compare with DPIP, our proposed Feature Preserving Loss is better. Feature Preserving Loss not only adaptively learns key features related to medical image reconstruction during the network training, but also quantifies the changes in features before and after denoising. Subsequently, by minimizing these changes, we can ensure that more important feature information for medical diagnostic can be retained during the denoising process.

In contrast, the classical denoising algorithms, such as Wiener filters, median filters or Gaussian filters, have difficulty

TABLE I: Summary of Noise and Artifacts Applied in our Experiment.

Noise or Artifact	Description
Chemical Shift (Chem. Shift)	An image artifact caused by differences in the chemical composition of different tissues.
Gaussian Noise (Gauss.)	A common type of image noise whose noise obeys a Gaussian distribution.
Magnetic Field Inhomogeneity (Mag. Field)	An image artifact due to uneven distribution of the magnetic field.
Motion Artifacts (Motion Art.)	Image artifacts caused by patient or organ motion during the scanning process.
Non-central Chi Noise (Non-cent. Chi)	A type of noise commonly found in magnetic resonance imaging (MRI).
Poisson Noise	Usually arises due to the inherent variability of photon counting.
Rician Noise (Rician)	A common noise in MRI images caused by fluctuations in the amplitude and phase of the signal.
Salt and Pepper Noise (Salt & Pepper)	Usually appears as random white and black dots in the image.
Speckle Noise	Noise due to interference of coherent light and is commonly seen in ultrasound images.
Structured Noise (Struct. Noise)	Usually generated by imperfections in scanning equipment or environmental disturbances.
Susceptibility Artifacts (Susc. Art.)	Result from inhomogeneities in the magnetic field or differences in the magnetization of a substance.
Thermal Noise (Thermal)	Random noise due to the thermal movement of electrons. Thermal noise may reduce the signal-to-noise ratio of an image, affecting the clarity of the image.
Wrap-around Artifacts (Wrap Around)	Caused by phase distortion during image reconstruction.

The contents of the parentheses will be used as abbreviations for Tables II, III and IV.

in maintaining denoising stability under different noise or artifacts conditions. This is due to the fact that classical denoising algorithms mainly rely on mathematical models to describe the relationship between images and noise. Therefore, they are usually manually designed for specific types of noise. In the case of the Wiener filter, the Wiener filter assumes that the image and the noise are linearly additive and tries to minimize the prediction error to estimate the original image. Thus, the Wiener filter tends to perform well when targeting a specific type of noise, such as salt and pepper noise. However, the Wiener filter becomes less effective at denoising when dealing with more complex or diverse noises.

Compared with other famous denoising algorithms, the superiority of our proposed method is demonstrated in the Structural Similarity Index (SSIM). SSIM assesses image quality from the perspective of human visual perception. On three different datasets, our method performs well on SSIM, ahead of other algorithms. This result not only validates the effectiveness of our loss function in feature preserving, but also shows that the method has a clear advantage in structural quality.

E. Qualitative Evaluation

Figures 3, 4 and 5 show the visual denoising results of our work. For each image, the first row from left to right shows: the clean image, the noisy image, our denoising result, and the DPIR denoising result. The second row from left to right

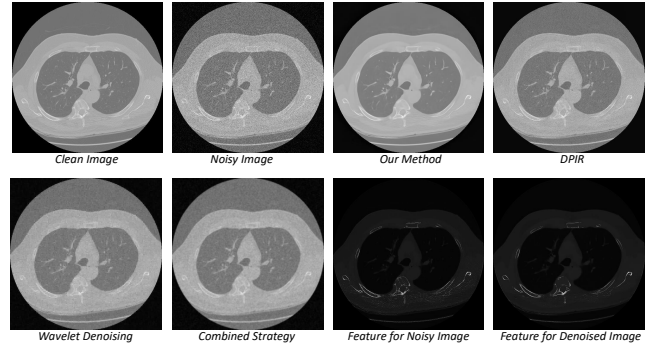


Fig. 3: Denoising Visualization Result for LIDC dataset as Gaussian Noise Applied.

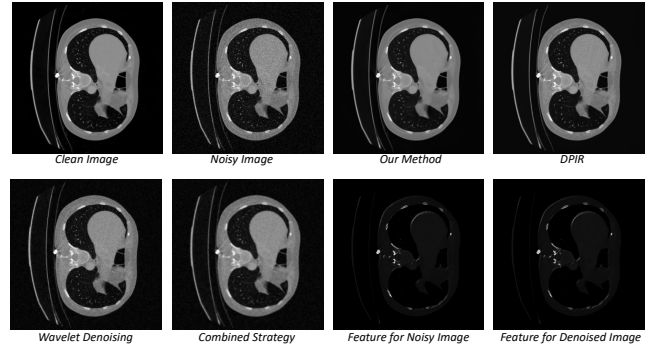


Fig. 4: Denoising Visualization Result for LiTs dataset as Gaussian Noise Applied.

are: result of Wavelet Denoising, result of Combine Strategy, feature of the noisy image, feature of the denoised image. Due to the length limitation, the noise we show in the Figures 3, 4 and 5 is Gaussian noise. The complete denoising results can be found in Google Drive¹. We will also publicly release the

¹<https://drive.google.com/drive/folders/17QxZauxFhdULcI1NpTDNNe8P4kx26Yab?usp=sharing>

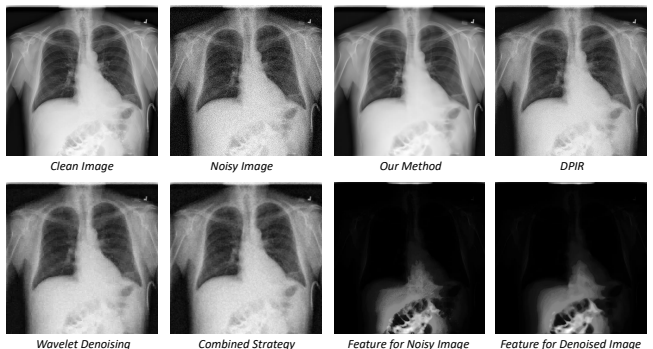


Fig. 5: Denoising Visualization Result for RSNA dataset as Gaussian Noise Applied.

TABLE II: LIDC PSNR and SSIM Comparison

	Noise Type	Our	DPIR	Bilat.	Filt. Comb.	Gaus. Filt.	Mean Filt.	Medi. Filt.	NL Mean.	Wave. Den.	Wien. Filt.
PSNR	Chem. Shift	49.39	35.95	36.01	35.70	35.82	35.74	35.99	35.65	35.61	34.79
	Gauss.	35.20	30.74	30.92	32.14	30.92	31.10	31.37	31.69	31.75	31.46
	Mag. Field	55.30	31.49	31.45	31.38	31.69	31.54	31.71	31.40	31.94	30.81
	Motion Art.	37.20	32.80	32.69	32.49	32.47	32.47	32.55	32.90	32.34	32.11
	Non-cent. Chi	32.17	27.55	27.53	27.28	27.38	27.36	27.47	27.92	27.34	28.19
	Poisson Noise	35.25	36.97	34.52	35.53	34.24	34.45	33.67	36.34	34.16	32.46
	Rician	33.88	29.73	29.32	30.35	29.62	29.75	29.45	30.50	30.30	30.61
	Salt & Pepper	38.60	36.08	36.68	32.60	33.18	32.53	41.10	38.86	41.50	31.73
	Speckle Noise	36.36	37.78	35.94	36.15	35.73	35.68	35.17	36.96	34.66	33.36
	Struct. Noise	30.54	27.99	27.98	27.97	27.97	27.97	27.97	28.01	27.99	28.18
	Susc. Art.	45.21	30.09	30.12	30.08	30.15	30.11	30.17	30.09	30.23	29.77
	Thermal	34.96	30.74	30.92	32.14	30.92	31.10	31.37	31.69	31.75	31.46
Wrap Around	35.26	31.57	31.48	31.35	31.35	31.34	31.41	31.60	31.28	31.12	
SSIM	Chem. Shift	0.98	0.83	0.83	0.84	0.83	0.83	0.82	0.82	0.81	0.66
	Gauss.	0.82	0.50	0.50	0.65	0.53	0.55	0.55	0.51	0.60	0.35
	Mag. Field	0.99	0.87	0.88	0.88	0.92	0.89	0.90	0.86	0.96	0.68
	Motion Art.	0.86	0.64	0.65	0.64	0.63	0.63	0.63	0.65	0.60	0.52
	Non-cent. Chi	0.76	0.13	0.14	0.45	0.30	0.32	0.29	0.25	0.41	0.26
	Poisson Noise	0.91	0.87	0.81	0.85	0.80	0.80	0.76	0.87	0.79	0.54
	Rician	0.81	0.46	0.45	0.60	0.49	0.50	0.45	0.50	0.56	0.37
	Salt & Pepper	0.88	0.29	0.27	0.63	0.46	0.47	0.92	0.32	0.29	0.31
	Speckle Noise	0.91	0.89	0.86	0.87	0.84	0.84	0.81	0.88	0.82	0.59
	Struct. Noise	0.83	0.55	0.55	0.56	0.58	0.56	0.57	0.53	0.61	0.50
	Susc. Art.	0.96	0.80	0.80	0.81	0.84	0.82	0.83	0.79	0.87	0.58
	Thermal	0.83	0.50	0.50	0.65	0.53	0.55	0.55	0.51	0.60	0.35
Wrap Around	0.82	0.59	0.60	0.59	0.58	0.58	0.58	0.60	0.56	0.48	

The full names of the abbreviations can be found in Table I and Section IV-D.

TABLE III: LiTs PSNR and SSIM Comparison

	Noise Type	Our	DPIR	Bilat.	Filt. Comb.	Gaus. Filt.	Mean Filt.	Medi. Filt.	NL Mean.	Wave. Den.	Wien. Filt.
PSNR	Chem. Shift	51.67	36.57	36.83	36.47	36.37	36.40	36.56	36.33	36.15	34.36
	Gauss.	37.40	31.13	31.37	31.99	31.00	31.15	32.01	31.70	31.66	32.24
	Mag. Field	55.12	34.02	33.79	33.65	34.24	34.00	34.50	33.77	34.50	32.15
	Motion Art.	39.58	34.36	34.25	34.01	34.01	34.01	34.12	34.37	33.97	32.82
	Non-cent. Chi	34.41	27.57	27.55	27.27	27.38	27.36	27.45	28.03	27.35	28.44
	Poisson Noise	39.41	39.70	36.18	37.16	36.08	36.30	35.47	37.77	34.18	33.42
	Rician	35.09	29.19	28.66	29.33	28.91	29.00	28.82	29.80	29.18	30.48
	Salt & Pepper	44.94	37.51	38.46	32.93	34.19	33.33	44.07	40.70	42.83	31.87
	Speckle Noise	39.84	40.21	37.76	37.80	37.79	37.67	37.35	38.93	35.05	34.12
	Struct. Noise	31.23	28.09	28.08	28.07	28.07	28.07	28.07	28.13	28.10	28.26
	Susc. Art.	47.52	33.03	33.01	32.95	33.29	33.15	33.32	32.88	33.37	31.90
	Thermal	36.99	31.13	31.37	31.99	31.00	31.15	32.01	31.70	31.66	32.24
Wrap Around	36.39	33.10	33.01	32.84	32.86	32.85	32.95	33.09	32.86	32.00	
SSIM	Chem. Shift	0.94	0.86	0.87	0.88	0.86	0.87	0.86	0.85	0.84	0.48
	Gauss.	0.85	0.52	0.51	0.64	0.52	0.55	0.59	0.45	0.57	0.28
	Impulse	0.89	0.30	0.29	0.62	0.44	0.46	0.98	0.32	0.30	0.25
	Mag. Field	0.99	0.92	0.92	0.93	0.96	0.95	0.95	0.89	0.95	0.52
	Motion Art.	0.85	0.76	0.76	0.75	0.74	0.74	0.74	0.75	0.72	0.40
	Non-cent. Chi	0.76	0.10	0.11	0.37	0.24	0.26	0.24	0.16	0.32	0.20
	Poisson Noise	0.94	0.93	0.87	0.92	0.87	0.88	0.84	0.92	0.79	0.44
	Rician	0.79	0.41	0.39	0.52	0.42	0.44	0.40	0.41	0.47	0.31
	Salt & Pepper	0.93	0.30	0.29	0.62	0.44	0.46	0.98	0.32	0.30	0.25
	Speckle Noise	0.95	0.94	0.92	0.93	0.91	0.91	0.89	0.92	0.82	0.47
	Struct. Noise	0.85	0.48	0.48	0.49	0.51	0.50	0.50	0.47	0.52	0.41
	Susc. Art.	0.98	0.85	0.86	0.86	0.88	0.88	0.88	0.82	0.87	0.47
Thermal	0.84	0.52	0.51	0.64	0.52	0.55	0.59	0.45	0.57	0.28	
Wrap Around	0.85	0.70	0.70	0.70	0.69	0.69	0.69	0.70	0.67	0.37	

The full names of the abbreviations can be found in Table I and Section IV-D.

TABLE IV: RSNA PSNR and SSIM Comparison

	Noise Type	Our	DPIR	Bilat.	Filt. Comb.	Gaus. Filt.	Mean Filt.	Medi. Filt.	NL Mean.	Wave. Den.	Wien. Filt.
PSNR	Chem. Shift	41.99	35.07	35.29	35.18	35.06	35.09	35.23	34.57	34.88	33.61
	Gauss.	34.65	30.12	30.11	31.77	30.38	30.63	30.26	30.47	31.23	29.50
	Mag. Field	49.86	30.11	30.12	30.15	30.25	30.21	30.28	29.95	30.31	29.69
	Motion Art.	34.47	31.29	31.22	31.14	31.11	31.11	31.12	31.34	31.03	30.81
	Non-cent. Chi	34.05	27.85	27.81	27.57	27.63	27.61	27.79	28.03	27.66	27.93
	Poisson Noise	35.80	32.47	31.55	33.03	31.62	31.89	31.25	32.91	31.55	29.82
	Rician	34.25	29.82	29.73	31.10	30.03	30.25	29.86	30.53	30.77	29.54
	Salt & Pepper	41.62	33.36	33.78	31.43	31.32	31.07	37.07	34.15	35.42	30.19
	Speckle Noise	36.11	32.83	32.09	33.21	32.13	32.33	31.82	32.84	31.20	30.05
	Struct. Noise	30.34	28.00	27.99	27.98	27.99	27.98	27.99	28.00	28.01	27.99
	Susc. Art.	42.88	29.80	29.81	29.86	29.97	29.93	30.01	29.67	30.10	29.61
	Thermal	34.75	30.12	30.11	31.77	30.38	30.63	30.26	30.47	31.23	29.50
Wrap Around	30.65	29.89	29.85	29.82	29.81	29.80	29.81	29.87	29.74	29.62	
SSIM	Chem. Shift	0.98	0.89	0.90	0.90	0.89	0.89	0.89	0.88	0.87	0.77
	Gauss.	0.91	0.55	0.55	0.81	0.63	0.67	0.60	0.69	0.78	0.42
	Mag. Field	0.99	0.91	0.91	0.93	0.96	0.95	0.95	0.89	0.97	0.77
	Motion Art.	0.95	0.75	0.75	0.74	0.72	0.73	0.72	0.76	0.71	0.65
	Non-cent. Chi	0.91	0.22	0.23	0.66	0.43	0.48	0.39	0.44	0.56	0.36
	Poisson Noise	0.94	0.78	0.72	0.87	0.74	0.77	0.71	0.90	0.77	0.49
	Rician	0.90	0.55	0.54	0.79	0.62	0.66	0.58	0.70	0.77	0.43
	Salt & Pepper	0.98	0.29	0.26	0.73	0.50	0.54	0.97	0.30	0.25	0.34
	Speckle Noise	0.95	0.81	0.77	0.89	0.79	0.81	0.75	0.90	0.71	0.54
	Struct. Noise	0.92	0.76	0.76	0.78	0.79	0.79	0.79	0.73	0.80	0.72
	Susc. Art.	0.99	0.82	0.82	0.84	0.86	0.85	0.86	0.80	0.87	0.72
	Thermal	0.92	0.55	0.55	0.81	0.63	0.67	0.60	0.69	0.78	0.42
Wrap Around	0.91	0.69	0.69	0.68	0.66	0.67	0.66	0.70	0.65	0.60	

The full names of the abbreviations can be found in Table I and Section IV-D.

code after the paper is accepted.

Overall, compared with other denoising algorithms, our method performs much better in terms of denoising performance. In particular, when compared with the DPIR, our method performs particularly well in terms of noise control. Our denoising results show almost no presence of granular noise points. Typically, the cost of eliminating granularity is that critical features in medical images may be over-smoothed or completely blurred. However, in our method, important feature regions in medical images can be effectively preserved with the help of Feature Preserving Loss.

As Figure 5 shows, for lung region, the DPIR algorithm result obviously lack a sense of hierarchy. The entire lung region is almost shows as a uniform white color. In contrast, our method successfully preserves the layering of the lung region guided by the feature preservation loss. Although there is a small difference compared to the clean image, our results can be still considered very satisfactory. Other visualization results also demonstrate the superiority of our method. As can be seen in Figure 3, our method performs much better in preserving the features of blood vessels and lesion regions compared to other algorithms. Considering the severe damage to the image by noise, our method has great potential to solve the feature preservation problem in denoising.

F. Discussion on Explainability

It is worth to mention that we do not claim to propose a new explainable method for medical images. The “medical image features” mentioned in this paper may differ from those in a real medical environment. The features we used are extracted from the reconstructed network by gradient-

based XAI method. These features quantify the importance of each input pixel in the reconstruction process. Although in most cases, the features extracted by XAI are consistent with those of the actual medical images (e.g., Figures 3, 4 and 5). However, due to the lack of guiding information, there is also a possibility of bias between the two.

In fact, a more ideal approach may be to train a medical image feature detection network with human annotation. The importance of these features is then further quantified by a gradient XAI method. However, due to the lack of labeled datasets, using an existing reconstructed network is a practical compromise. Despite the possible differences in features between the two, our denoising results still demonstrate excellent performance and effective feature preserving ability. This further confirms that utilizing feature preserving loss is a correct strategy. In the future, we will focus on obtaining more accurate features.

V. CONCLUSION

In this work, we purposed a new loss function called Feature Preserving Loss that helps denosing network preserving medical features essential for diagnosis. This new loss function exploits the capabilities of gradient-based eXplainable Artificial Intelligence (XAI) and leverages the sensitivity of gradient-based XAI methods to noise. Notably, this approach not only excels in denoising but also enhances the explainability of the model by visualizing the feature map. Future research can focus on obtaining more accurate medical features. Overall, we present an effective and explainable denosing method, which has the great potential for application in medical image denoising.

REFERENCES

- [1] A. Kaur and G. Dong, "A complete review on image denoising techniques for medical images," *Neural Processing Letters*, pp. 1–44, 2023.
- [2] B. H. Van der Velden, H. J. Kuijff, K. G. Gilhuijs, and M. A. Viergever, "Explainable artificial intelligence (xai) in deep learning-based medical image analysis," *Medical Image Analysis*, vol. 79, p. 102470, 2022.
- [3] K. R. Castleman, *Digital image processing*. Prentice Hall Press, 1996.
- [4] T. Huang, G. Yang, and G. Tang, "A fast two-dimensional median filtering algorithm," *IEEE transactions on acoustics, speech, and signal processing*, vol. 27, no. 1, pp. 13–18, 1979.
- [5] J. Canny, "A computational approach to edge detection," *IEEE Transactions on pattern analysis and machine intelligence*, no. 6, pp. 679–698, 1986.
- [6] T. Kailath and T. Kailath, *Lectures on Wiener and Kalman filtering*. Springer, 1981.
- [7] D. L. Donoho and I. M. Johnstone, "Adapting to unknown smoothness via wavelet shrinkage," *Journal of the american statistical association*, vol. 90, no. 432, pp. 1200–1224, 1995.
- [8] K. Dabov, A. Foi, V. Katkovnik, and K. Egiazarian, "Image denoising by sparse 3-d transform-domain collaborative filtering," *IEEE Transactions on image processing*, vol. 16, no. 8, pp. 2080–2095, 2007.
- [9] K. Zhang, Y. Li, W. Zuo, L. Zhang, L. Van Gool, and R. Timofte, "Plug-and-play image restoration with deep denoiser prior," *IEEE Transactions on Pattern Analysis and Machine Intelligence*, vol. 44, no. 10, pp. 6360–6376, 2021.
- [10] R. Neshatavar, M. Yavartanoo, S. Son, and K. M. Lee, "Cvf-sid: Cyclic multi-variate function for self-supervised image denoising by disentangling noise from image," in *Proceedings of the IEEE/CVF Conference on Computer Vision and Pattern Recognition*, 2022, pp. 17 583–17 591.
- [11] G. Dong, Y. Ma, and A. Basu, "Feature-guided cnn for denoising images from portable ultrasound devices," *IEEE Access*, vol. 9, pp. 28 272–28 281, 2021.
- [12] J. Springenberg, A. Dosovitskiy, T. Brox, and M. Riedmiller, "Striving for simplicity: The all convolutional net," in *ICLR (workshop track)*, 2015.
- [13] K. Simonyan, A. Vedaldi, and A. Zisserman, "Deep inside convolutional networks: Visualising image classification models and saliency maps," *arXiv preprint arXiv:1312.6034*, 2013.
- [14] R. R. Selvaraju, M. Cogswell, A. Das, R. Vedantam, D. Parikh, and D. Batra, "Grad-cam: Visual explanations from deep networks via gradient-based localization," in *Proceedings of the IEEE international conference on computer vision*, 2017, pp. 618–626.
- [15] D. Smilkov, N. Thorat, B. Kim, F. Viégas, and M. Wattenberg, "Smoothgrad: removing noise by adding noise," *arXiv preprint arXiv:1706.03825*, 2017.
- [16] M. Sundararajan, A. Taly, and Q. Yan, "Axiomatic attribution for deep networks," in *International conference on machine learning*. PMLR, 2017, pp. 3319–3328.
- [17] O. Ronneberger, P. Fischer, and T. Brox, "U-net: Convolutional networks for biomedical image segmentation," in *Medical Image Computing and Computer-Assisted Intervention–MICCAI 2015: 18th International Conference, Munich, Germany, October 5–9, 2015, Proceedings, Part III 18*. Springer, 2015, pp. 234–241.
- [18] S. G. Armato III, G. McLennan, L. Bidaut, M. F. McNitt-Gray, C. R. Meyer, A. P. Reeves, B. Zhao, D. R. Aberle, C. I. Henschke, E. A. Hoffman *et al.*, "The lung image database consortium (lidc) and image database resource initiative (idri): a completed reference database of lung nodules on ct scans," *Medical physics*, vol. 38, no. 2, pp. 915–931, 2011.
- [19] X. Wang, Y. Peng, L. Lu, Z. Lu, M. Bagheri, and R. M. Summers, "Chestx-ray8: Hospital-scale chest x-ray database and benchmarks on weakly-supervised classification and localization of common thorax diseases," in *Proceedings of the IEEE conference on computer vision and pattern recognition*, 2017, pp. 2097–2106.
- [20] P. Bilic, P. Christ, H. B. Li, E. Vorontsov, A. Ben-Cohen, G. Kaissis, A. Szeskin, C. Jacobs, G. E. H. Mamani, G. Chartrand *et al.*, "The liver tumor segmentation benchmark (lits)," *Medical Image Analysis*, vol. 84, p. 102680, 2023.